Mon. Not. R. Astron. Soc. **349,** 779–792 (2004) doi:10.1111/j.1365-2966.2004.07597.x

Synchrotron nebulae created by anisotropic magnetized pulsar winds

S. S. Komissarov[1]★ and Y. E. Lyubarsky[2]★

[1]*Department of Applied Mathematics, University of Leeds, Leeds LS2 9JT*
[2]*Physics Department, Ben-Gurion University, PO Box 653, Beer-Sheva 84105, Israel*

Accepted 2004 January 5. Received 2003 December 17; in original form 2003 September 10

ABSTRACT

In this paper, we give a detailed description of the first attempt to study the properties of the flow produced by a magnetized pulsar wind within a plerionic nebula via fully relativistic magnetohydrodynamic (MHD) simulations. Following the current theoretical models of pulsar winds, we assume that in the equatorial direction the magnetization of the wind drops to zero but its energy flux reaches a maximum. The results of our 2D axisymmetric simulations reveal complex dynamics of the post-shock flow, very different from the steady quasi-radial outflow assumed in earlier analytical models for plerions. The termination shock has the shape of a distorted torus and most of the downstream flow is initially confined to the equatorial plane. Provided the wind magnetization is higher than a certain value, the magnetic hoop stress stops the outflow in the surface layers of the equatorial disc and redirects it into magnetically confined polar jets. The outflow in the inner layers of the equatorial disc continues until it reaches the slowly expanding outer shell and then turns back and forms the vortex flow filling the nebular volume at intermediate latitudes. We simulated the synchrotron images of the nebula taking into account the relativistic beaming effect and the particle energy losses. These images are strikingly similar to the well-known images of the Crab and other pulsar wind nebulae obtained by *Chandra* and the *Hubble Space Telescope*. They exhibit both a system of rings, which makes an impression of an equatorial disc-like or even a toroidal structure, and well-collimated polar jets, which appear to originate from the pulsar. A number of fine details of the inner Crab nebula find natural explanation including the bright knot discovered by Hester et al. in 1995 very close to the Crab pulsar.

Key words: MHD – shock waves – pulsars: general – ISM: individual: Crab nebula – ISM: jets and outflows – supernova remnants.

1 INTRODUCTION

The nature of synchrotron-emitting plerionic nebulae found in many supernova remnants (Weiler & Panagia 1978) has been the subject of intense research for many decades, the Crab nebula being the best-studied and most well-known example. It is now commonly accepted that such nebulae are produced by a relativistic magnetized wind from the rotating neutron star formed inside the supernova remnant during the supernova explosion. As the wind velocity is very close to the speed of light, but the expansion of the surrounding massive stellar envelope is much slower, the pulsar wind terminates at a strong reverse shock and the shocked plasma fills the interior of the envelope. The observed synchrotron emission is explained by the conversion of the wind energy into the energy of relativistic particles and magnetic field at the termination shock. This general idea was developed into a quantitative model by Rees & Gunn (1974) and Kennel & Coroniti (1984) and was elaborated even further by Emmering & Chevalier (1987) and Begelman & Li (1992). Since direct observations of pulsar winds were, and still remain, rather problematic (cf. Kirk, Ball & Skj 1999; Bogovalov & Aharonian 2000; Kirk, Skjæraasen & Gallant 2002), and in order to simplify the calculations, these authors made the most convenient assumption on the angular distribution of the wind power, namely that it is isotropic.

The steady progress of X-ray astronomy has resulted in the discovery of a rather peculiar structure in the inner part of the Crab nebula, not expected in the classical models of plerions. This so-called 'jet–torus' structure had already been seen in earlier observations by Brinkmann et al. (1985) and Hester et al. (1995), but the recent *Chandra* data show this structure in greater detail (Weisskopf et al. 2000; Hester et al. 2002). As similar structures have been found in other pulsar wind nebulae (Helfand, Gotthelf & Halpern 2001; Pavlov et al. 2001; Gaensler, Pivovaroff & Garmire 2001; Gaensler et al. 2002; Lu et al. 2002), this is likely to be a generic phenomenon. The Crab 'torus' is the most prominent component of the structure.

★E-mail: serguei@maths.leeds.ac.uk (SSK); lyub@bgumail.bgu.ac.il (YEL)

Whether this is really a torus or rather a disc normal to the rotational axis of the pulsar is not yet clear, but its mere existence suggests a high degree of anisotropy of the MHD flow in the inner part of the Crab nebula, which has to be related to the anisotropy of the pulsar wind itself.

Although no comprehensive theory of the relativistic winds from obliquely rotating pulsars yet exists, the available idealized models show that such winds are likely to be highly anisotropic, with most of the energy flowing out near the equatorial plane. Indeed, in the axisymmetric split-monopole solution for the aligned rotator (Michel 1973), the Poynting flux is proportional to $\sin^2\theta$, where θ is the polar angle. Such a distribution is a natural feature of axisymmetric MHD flows because in the far zone the magnetic field is almost azimuthal and, thus, must vanish at the symmetry axis (Ingraham 1973; Michel 1974). The situation is less clear for the winds from oblique rotators; however, the results of Bogovalov (1999) suggest that the angular distribution of their Poynting flux may not be all that different after all.

Using the approximation of constant post-shock pressure, Lyubarsky (2002) and Bogovalov & Khangoulyan (2002a) have already studied some properties of the termination shock of the split-monopole wind. They found that the shock has the shape of a torus aligned with the symmetry axis. These results strongly support the idea that the origin of the Crab torus has to be sought in the anisotropy of the pulsar wind. Bogovalov & Khangoulyan (2002b) also modelled the synchrotron emission from the post-shock region, assuming a constant-pressure radial flow. However, this assumption is hard to justify as the termination shock is very oblique at high latitudes. This seems to be one of the reasons why their simulated images are too wide and diffusive compared to the observations.

The jet of the Crab nebula, as well as the jets of other pulsars, appears to originate from the pulsar and to propagate along the rotational axis. This seems to indicate that they are formed within the pulsar wind and collimation by magnetic hoop stress suggests itself. However, such a collimation is found to be extremely ineffective in ultrarelativistic flows (Tomimatsu 1994; Beskin, Kuznetsova & Rafikov 1998; Chiueh, Li & Begelman 1998; Bogovalov & Tsinganos 1999; Bogovalov 2001; Lyubarsky & Eichler 2001). Moreover, jets of such origin would have to be ultrarelativistic whereas the observed jets are certainly not. Indeed, the mere fact that both the jet and the counter-jet are seen in the images of the Crab and the Vela nebulae (Weisskopf et al. 2000; Helfand et al. 2001) alone rules out ultrarelativistic speeds. Moreover, direct observations of the proper motion in the Crab and Vela jets indicate rather moderate velocities of $\approx$(0.3–0.7)c only (Hester et al. 2002; Pavlov et al. 2003). These problems stimulated recent attempts to find alternative explanations of the pulsar jets.

Bogovalov & Khangoulyan (2002b) interpreted the nebula jets as high particle density polar regions of the flow downstream of the termination shock. In their purely hydrodynamical model, there is no pressure and energy density excess at the axis; the particle density increases towards the axis only because the particle energy decreases. It is difficult to see how this enhanced density of low-energy particles ($\sim$100 MeV in their model) can result in higher synchrotron emissivity in the X-ray band. Moreover, their analysis is too hampered by the assumption of constant-pressure radial post-shock outflow.

Lyubarsky (2002) pointed out that, although the magnetic collimation is futile in the pulsar wind itself, it becomes much more effective downstream of the termination shock where the flow is no longer ultrarelativistic and proposed that the Crab jet could be formed via magnetic collimation in this region. In his model, the observed jet-like feature arises naturally because of the axial compression of the synchrotron-emitting plasma. The jet appears to originate from the pulsar simply because the termination shock is much closer to the wind origin along the symmetry axis. There is no way of testing this hypothesis other than to solve the problem of interaction between a highly anisotropic, relativistic, magnetized wind and its environment, which could be a supernova ejecta or interstellar medium (ISM). However, this problem is too complicated for modern analytical techniques and only numerical simulations can provide us with required answers. Fortunately, dramatic progress in numerical methods for relativistic gas dynamics and MHD in recent years has made such an approach possible (Marti & Muller 1999; Komissarov 1999a). In Komissarov & Lyubarsky (2003) we briefly described the results of the first ever such study. In this article we give a detailed account of it.

In Section 2 we describe the basic assumptions of our mathematical model. Section 3 outlines the main features of our numerical technique and the setup of simulations. The results of simulations are described in Section 4. To make direct comparison with the observations, we need to model the synchrotron emission from the nebula. This model and the simulated synchrotron images are described in Section 5. The implication of our results for the theory of plerions is discussed in Section 6. The final section (Section 7) summarizes our conclusions.

2 THE MODEL

To set up the simulations we need to specify both the pulsar wind and the surrounding medium with which this wind is interacting. Here we describe rather simplified models for these two components, which by no means represent the full complexity of the real phenomena and undoubtedly will be revised in the future. However, they seem to be quite adequate to the present level of our understanding of this problem.

2.1 Pulsar wind

It is widely believed that the relativistic magnetized winds from neutron stars can be described as axisymmetric, supermagnetosonic radial outflows with purely azimuthal magnetic field (e.g. Chiueh et al. 1998). The only global solutions currently available for pulsar winds assume the split-monopole topology of magnetic field (Michel 1973; Bogovalov 1999). Although real winds are likely to be more complex, we believe that the split-monopole solutions capture, at least qualitatively, some of their main properties. For example, these solutions have a highly anisotropic distribution of the energy flux that may explain the origin of the observed X-ray tori in plerionic nebulae (Lyubarsky 2002; Bogovalov & Khangoulyan 2002a).

Therefore we assume the same distribution of the total energy flux, $f_{\rm tot}$, as in the split-monopole solution, namely

$$f_{\rm tot} = (f_0/r^2)(\sin^2\theta + 1/\sigma_0), \qquad (1)$$

where r and θ are the usual spherical coordinates. The first term in the brackets represents the Poynting flux whereas the second one accounts for the small initial contribution of the wind particles. At larger distances, a significant part of the Poynting flux may be converted into kinetic energy but the total energy per particle is conserved along the streamlines and, thus, the angular distribution (1) remains unchanged. However, the asymptotic distributions of magnetic field, density and velocity in the wind do depend on details of the conversion mechanism. Although this mechanism remains a

subject of ongoing debate, a number of recent results seem to give us a clue of what it could be.

When considering the energy conversion in the pulsar wind, one should take into account the fact that pulsars are oblique rotators, i.e. their magnetic axis is inclined with respect to their rotation axis. Close to the pulsar, the Poynting flux is transported partly by the oscillating component of the electromagnetic field and partly by its mean component. In the polar region, where the magnetic field does not alternate, the oscillating component has the form of a fast magnetosonic wave. Owing to non-linear steepening and subsequent formation of multiple shocks, such waves decay and transfer their energy to particles. Lyubarsky (2003a) found that, in the case of a rapidly spinning pulsar, such as the Crab pulsar, these waves may have decayed well before the termination shock.

In the equatorial region, the magnetic field alternates, being connected to a different magnetic pole every half-period. Such a flow is known as the striped wind (Michel 1971; Bogovalov 1999). The electromagnetic energy of the striped wind dissipates because of current starvation in the current sheets separating strips with opposite magnetic field (Usov 1975; Michel 1982, 1994; Coroniti 1990; Lyubarsky & Eichler 2001; Kirk & Skjæraasen 2003). The dissipation scale may exceed the termination shock radius. However, when the striped wind enters the shock, the alternating field immediately annihilates and the post-shock parameters take the same values as if the alternating field had annihilated already in the upstream flow (Lyubarsky 2003b). Thus, in our study of the MHD flow in the vicinity of the termination shock, we may safely assume that all the waves have already decayed and transferred their energy to the particles. In such a case, the mean magnetic field is no longer described by the simple $\sin\theta$ dependence on the polar angle but vanishes at $\theta = \pi/2$ as well.

To account for these properties of the pulsar wind we assume that its magnetic field satisfies the equation

$$B = \sqrt{\frac{4\pi f_0}{c}}\frac{\xi}{r}\sin\theta\left(1-\frac{2\theta}{\pi}\right) \tag{2}$$

for $\theta \leqslant \pi/2$, where B is the magnetic field as measured by the fiducial inertial observer at rest relative to the pulsar. The free parameter $\xi \leqslant 1$ controls the magnetization of the wind. The kinetic energy flux of such a wind is then found as

$$f_{\rm k} \equiv \rho c^2 \gamma v = f_{\rm tot} - (B^2/4\pi)c, \tag{3}$$

where ρ is the mass density as measured in the flow frame, and v and γ are the wind velocity and Lorentz factor as measured by the fiducial observer. For the ultrarelativistic flow, $v \to c$, the post-shock plasma is relativistically hot and the dynamics of the downstream flow depends only on the product $\rho\gamma$. Therefore, the angular distributions of density and velocity in the wind may be chosen quite arbitrarily provided the product $\rho\gamma$ is fixed.

2.2 External medium

In the classical model of the Crab nebula it is assumed that the pulsar wind is confined by its supernova remnant (Kennel & Coroniti 1984). Although this assumption seems quite natural, the observational evidence for such a remnant has been surprisingly scarce (Sankrit & Hester 1996). This could be explained if the Crab supernova exploded in a very rarefied environment and its ejecta had been freely expanding ever since. Therefore, we assume that the nebula is confined by cold and dense plasma expanding with constant velocity $v_{\rm c}$. In addition, we totally ignore the line-emitting filaments of the Crab nebula. Their total mass is about 1–2 solar masses and they are likely to be dynamically important. However, we had to ignore them in order to keep the problem relatively simple.

Under such conditions and the assumption of a steady pulsar wind, the nebula has to evolve in a self-similar fashion (Emmering & Chevalier 1987). Such a property is very welcome as it suggests a clear strategy for the numerical experiment. The simulations can be terminated as soon as the numerical solution has more or less settled to this self-similar pattern. There is little sense in continuing them further as not much additional information can be obtained after this point. After this, the solution can be compared with observations by means of simple scaling.

During the self-similar phase the characteristic length scale grows linearly with time, $r \propto t$, whereas the gas pressure and magnetic field vary as

$$p,\, B^2 \propto W v_{\rm c}^{-3} t^{-2} \propto W v_{\rm c}^{-1} R_{\rm c}^{-2}, \tag{4}$$

where W is the wind power and $R_{\rm c}$ is the size of the nebula.

3 NUMERICAL METHOD AND SETUP OF SIMULATIONS

To carry out these simulations we used essentially the same second order in space and time Godunov-type scheme for relativistic MHD as described in Komissarov (1999a) and later used in numerical studies of relativistic MHD jets (Komissarov 1999b). The main modifications include (1) explicit reduction of the scheme to first order in both space and time for strong shocks and (2) the introduction of a variable time-step adjusted to the properties of a spherical grid.

We had to reduce the scheme to first order because we found that the original second-order scheme could not handle strong ultrarelativistic shocks that were stationary relative to the computational grid unless the magnetization of the flow was rather weak.

The radial nature of streamlines in the pulsar wind suggests utilization of spherical coordinates $\{\phi, r, \theta\}$. However, on a spherical grid with fixed angular size $\Delta\theta$ of computational cells, their spatial size $\Delta r_i = r_i\Delta\theta$ grows like r. As the Courant time-step stability condition requires $\Delta t < \Delta r_i/c$, the time-step suitable for the outer part of the computational domain can be much larger than that for its inner part. To reduce the computational cost, we split the computational domain into a set of rings such that the outer radius of each ring is twice its inner radius and advanced the solution separately for each kth ring with its own time-step, Δt_k, such that $\Delta t_{k+1} = 2\Delta t_k$. As a result, the outer regions of the computational domain are progressively less expensive in terms of computational time.

The basic components of this numerical scheme were subjected to rigorous testing as described in Komissarov (1999a). A number of additional simulations have been carried out to test the simple modifications dictated by the nature of the spherical grid. Non-magnetic test problems included the standard problems of spherical and cylindrical blast waves, as well as the problem of a spherically symmetrical wind with standing termination shock. In the magnetic regime we considered the Z-pinch problem using the equilibrium solution described in Komissarov (1999b). This configuration is known to be unstable and the solution is expected to stay near equilibrium only for a time comparable with the sound crossing time (e.g. Begelman 1998). The results of computer simulations are fully consistent with such expectations.

Table 1 contains the values of the main parameters of these simulations, and our choice of some of them requires an explanation. The ratio of the shock dimensions along the polar axis, $R_{\rm p}$, and the

Table 1. Parameters of numerical models.

Wind power constant	f_0	1.0
Wind asymmetry constant	σ_0	10
Wind Lorentz factor	γ_w	10
Wind magnetization parameter	ξ	0.0, 0.2, 0.3, 0.5
Envelope speed	v_e	0.017
Envelope density	ρ_e	10^4
Inner grid boundary	r_0	0.2, 0.1, 0.1, 0.04
Initial cavity radius	r_c	2.0
Ratio of specific heats	Γ	4/3

equatorial plane, R_{eq}, may be estimated as

$$R_p/R_{eq} \sim 1/\sqrt{1+\sigma_0}. \quad (5)$$

This follows from the results obtained in Lyubarsky (2002) under the assumption of uniform pressure downstream of the termination shock. Thus, for the widely accepted value of $\sigma_0 = 10^4$ for the Crab pulsar, the equatorial size of the termination shock is expected to be 100 times larger than its size along the polar axis. In fact, the results of our simulations show that equation (5) underestimates this ratio by a factor of 2–3, as the total downstream pressure near the axis is significantly higher due to the magnetic pinch of the shocked plasma. The anisotropy of the termination shock determines the range of linear scales required both to capture the large-scale structure of the flow in the plerionic nebula and to ensure that the whole of the termination shock is inside the computational domain. If the polar part of the termination shock becomes submerged into the central hole of the grid, this can be handled by switching to the 'solid wall' boundary condition in the corresponding polar region of the inner boundary which prevents plasma from sinking below $r = r_0$. This makes sense because even if the shock dives all the way down to the star surface the relativistically hot plerion plasma cannot be accreted by the pulsar. Obviously, the solution will be distorted as a result, but, provided this polar region is relatively small, the distortion is expected to be rather limited. Indeed, most of the energy is carried out by the wind in the equatorial direction. Initially, we used $\sigma_0 = 100$ and utilized the solid wall boundary in the polar region. Later, as this approach met with criticism, we reduced σ_0 down to 10 and also reduced r_0 ensuring that the whole of the termination shock was inside the computational domain. This noticeably increased the computational cost but the outcome turned out to be very similar. In this paper, we only present results for $\sigma_0 = 10$.

As we have explained in Section 2 the flow dynamics does not depend much on the exact value of the wind's Lorentz factor as long as it remains much larger than 1. On the other hand, too high a value of γ is not easy to deal with in this numerical scheme. The adopted value of $\gamma = 10$ seems to be a reasonable compromise.

The range of ξ covered in our simulations allows one to trace the transition from the 'jet–torus' morphology to the 'lonely torus' morphology of numerical solutions (see Section 4). In the pulsar literature, the wind magnetization is typically measured by parameter σ, defined as the ratio of the Poynting flux to the kinetic energy flux (e.g. Kennel & Coroniti 1984). According to equations (2) and (3), the local value of σ is zero at the equator, reaches the maximum value of $\sigma = \xi^2$ near the symmetry axis, and then sharply decreases to zero at the axis. The mean value of σ, defined as the ratio of the total energy transported by the electromagnetic fields to the total energy transported by the particles, is

$$\sigma_m = c\langle B^2\rangle/4\pi\langle f_k\rangle \approx 0.1\xi^2. \quad (6)$$

For the values of ξ given in Table 1, one has $\sigma_m = 0, 4\times10^{-3}, 9\times10^{-3}$ and 2.5×10^{-2}, respectively. These values are comparable with the earlier estimates based on highly simplified analytical or semi-analytical models (Kennel & Coroniti 1984; Emmering & Chevalier 1987; Begelman & Li 1992).

In order to account for the expanding envelope surrounding the plerion, the initial solution includes a cold, dense, uniform, unmagnetized plasma of mass density $\rho_e = 10^4$ and radial velocity $v_e = 0.017c$ ($= 5000$ km s^{-1}). This density is about 10^6 times higher than the typical proper density of the wind at $r = 1$. For such a high value, the plerion cavity is forced to expand with speed close to v_e. In fact, the resultant value of $v_c \simeq (0.02$–$0.03)c$ is still $\approx$3–4 times higher than the mean expansion speed of the Crab nebula, $0.007c$ ($= 2000$ km s^{-1}), deduced from the observations. Such high values of v_c resulted in further decrease of the computational cost. Fortunately, scalings like equation (4) can be used to evaluate the effect of lowering v_c.

The results of the simulations will be presented in dimensionless form such that the speed of light is $c = 1$. In order to scale the results to the spatial size of the Crab nebula, the appropriate unit of length is $L_0 = (1/3)$pc $= 10^{18}$ cm and the corresponding unit of time is then $T_0 = 1$yr $= 3\times10^7$ s. The unit of mass required to scale the wind power to the observed spin-down power of the Crab pulsar, 5×10^{38}ergs^{-1}, is $M_0 = 6.6\times10^{24}$ g. The corresponding unit of magnetic field is then $B_0 = 4.4\times10^{-5}$ G.

The initial radius of the plerion cavity, r_c, is significantly higher than the inner radius of the computational domain in order to ensure that the termination shock is not pushed back out of the domain soon after the start of simulations. At $t = 0$, the region with $r < r_c$ is filled with the unshocked pulsar wind and, thus, the initial solution is far from the desired self-similar phase. The transition is expected to take place when the cavity volume becomes much larger than its initial value.

The main cost-reducing factor is, of cause, the condition of exact axisymmetry. We believe that this is a severe constraint that one must always keep in mind when making comparisons between the results of 2D simulations with real 3D phenomena. Some features are expected to be artificially strengthened whereas others are expected to be prohibited altogether. Moreover, we also imposed the symmetry boundary condition in the equatorial plane, thus reducing the computational cost by another factor of 2.

The simulations were carried out in two steps. During the first step, up to $t = 140$, the computational grid has 80 cells in the θ direction and 240 cells in the radial direction. By the end of this stage, the numerical solution seems to approach the self-similar regime. During the second stage, up to $t = 190$, the numerical resolution is higher by a factor of 2, thus allowing us to study the central region of the flow in greater detail.

4 FLOW DYNAMICS

Fig. 1 shows the evolution of the $\xi = 0.5$ model during the first stage of the simulations (at lower resolution). One can see that it proceeds more or less in agreement with the results of Begelman & Li (1992). Indeed, with the exception of the central region around the termination shock the total pressure depends mainly on the cylindrical radius, $w = r\sin\theta$, and reaches a maximum on the symmetry axis. Such pressure distribution leads to a somewhat higher expansion speed in the axial direction, which results in the noticeable elongation of the nebula.

The origin of the small bumps in the equatorial plane is somewhat different. As one can see in Fig. 2, which shows the solution by the

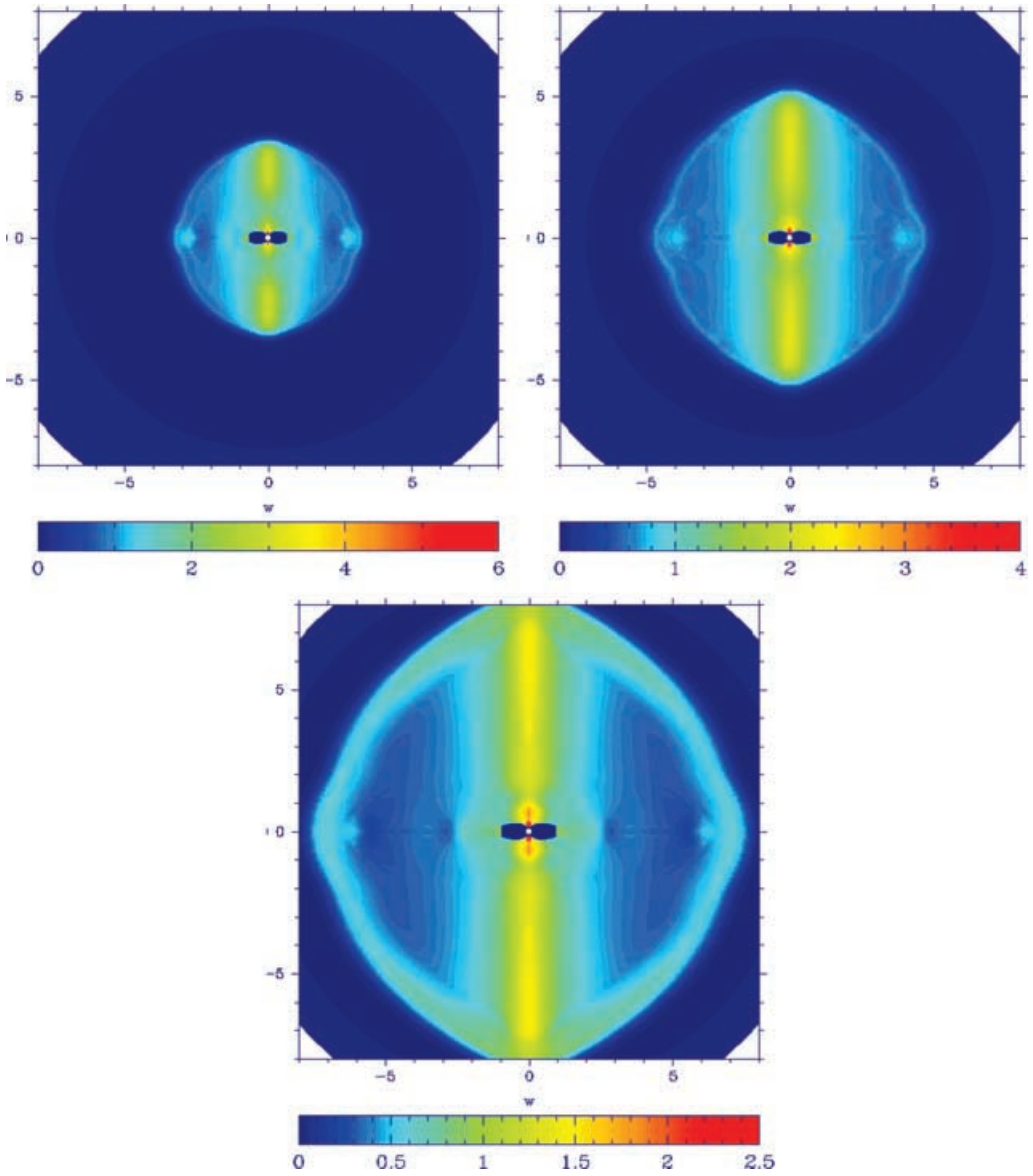

Figure 1. Total pressure distribution for the $\xi = 0.3$ model at $t = 40$ (top left), 90 (top right) and 140 (bottom).

end of the second stage, at $t = 190$, the outflow from the termination shock is not radial, as assumed in the classical model of pulsar nebulae (Kennel & Coroniti 1984; Emmering & Chevalier 1987) and in many other studies (e.g. Bogovalov & Khangoulyan 2002a,b; Bucciantini et al. 2003; van der Swaluw 2003; Shibata et al. 2003), but mostly confined to the equatorial plane. The typical velocity of the equatorial outflow is about $0.6c$, which is only slightly less than the local magnetosonic speed. Such a high velocity means high ram pressure of the outflow and this explains the origin of the equatorial bumps. Moreover, the speed of the equatorial outflow is much higher than the expansion speed of the nebula, and plasma supplied by the outflow into the bump region is then pushed back into the cavity. This must be the origin of the large-scale backflow just above and below the equatorial outflow which is clearly seen in Fig. 2. Its velocity is still quite high, $(0.1–0.3)c$, and when it reaches the central region it forms another outflow that eventually creates a large-scale vortex inside the nebula at intermediate latitudes. Within $r = 0.5$ one can see another thin backflow originating from the surface of the equatorial outflow. The nature of this backflow, which is quite different from the nature of the large-scale backflow, will be explained later.

Another remarkable feature of Fig. 2 is the two highly collimated polar jets whose velocity, $v_j \approx 0.5c$, is also only slightly lower than the local magnetosonic speed. In all models where these jets are observed they appear at a very early stage of simulations, around $t = 10$, and then remain a permanent feature of the solution. We will discuss the origin of these jets later in this section.

The left panel of Fig. 2 shows the ratio of the magnetic pressure to the gas pressure. This ratio is highest in the surface layers of the equatorial outflow, reaching there values of 2–3, whereas in the main volume of the nebula it is around 0.5–1. Such high values indicate that the magnetic field plays an important dynamical role in the evolution of the nebula.

Fig. 3 provides more detailed information about the central part of this solution by the end of the second stage of the simulations (at higher resolution). The pressure plot reveals a rather complicated structure of the wind termination shock. In fact, this is not a single

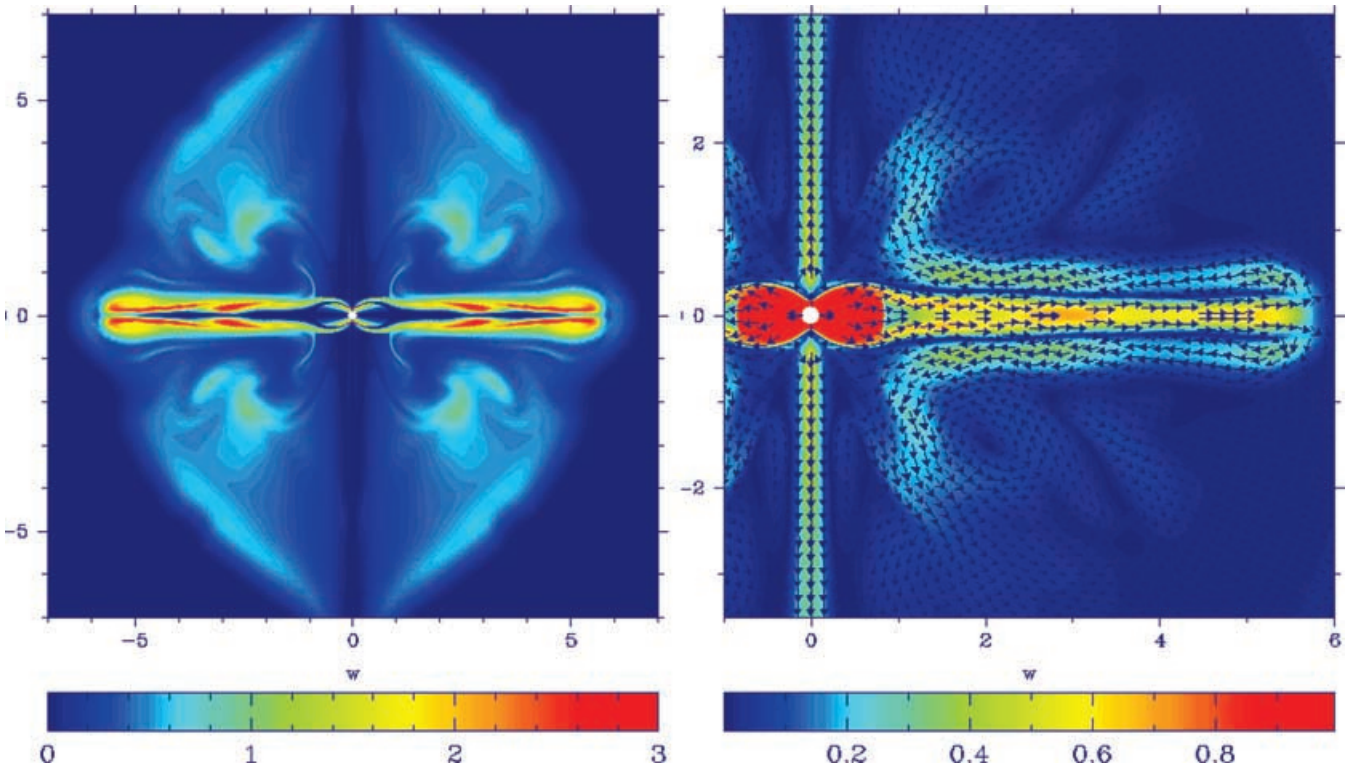

Figure 2. The $\xi = 0.3$ model at $t = 190$. Left panel: Ratio of magnetic to gas pressures, p_m/p_g. Right panel: Magnitude and direction of velocity.

shock but a complex of five shocks originating from two parallel junction circles located at $(z, w) = (\pm 0.1, 0.6)$. We shall refer to the shock connecting this junction with the polar axis as the 'arch shock', to the almost cylindrical shock crossing the equator as the 'Mach belt', whereas the remaining relatively weak and short shock making the angle around 45° with the equatorial plane will be called the 'rim shock'.

The flow passes the arch shock at a rather oblique angle and remains supermagnetosonic, with the typical speed being around $(0.8–0.9)c$, until it passes through the rim shock. Such a high velocity means that any emission from this region is subject to strong Doppler beaming. We shall call this high-velocity outflow just above the arch shock the 'Υ stream'. Downstream of the rim shock both the gas pressure and the magnetic pressure reach a local maximum.

As one can see in Fig. 3, the magnetic field is particularly strong near the outer boundary of the Υ stream. In fact, the Υ stream consists of streamlines originating from different sections of the arch shock. As we move away from the shock across the Υ stream, we meet streamlines that are progressively closer to the polar axis in the wind zone. Since the local magnetization of the wind, σ, mainly increases towards the polar axis, so does the ratio of the magnetic pressure to the gas pressure in the post-shock state. As a result, the outer layers of the Υ stream are most affected by the magnetic force.

Fig. 3 also explains the origin of the inner backflow and the polar jets which are already seen in Fig. 2. Clearly, the inner backflow is fed by the surface layers of the equatorial outflow. This is because the magnetic hoop stress in the surface layers is so strong that it first stops the outflow and then forces its plasma to flow back towards the symmetry axis. Eventually, as the backflow converges towards the axis, the hoop stress of its magnetic field creates strong compression in the region just above the cusp of the arch shock and, hence, drives the outflow in the polar direction. Thus, the polar jets are pressure-driven and magnetically collimated. Our conclusion on the role of magnetic field in the jet formation is supported by the results presented in Fig. 4. Once the value of the wind magnetization parameter ξ becomes as low as $\xi = 0.2$, fast polar jets are no longer produced.

Another interesting result seen in Fig. 4 is the dependence of the termination shock on the wind magnetization. Whereas the size of the whole nebula is approximately the same for all our models, the size of the termination shock significantly decreases with ξ, in general agreement with the results obtained in Emmering & Chevalier (1987). The self-similar solution of Emmering & Chevalier exists only for $\sigma < v_c/(c - v_c)$, where v_c is the velocity of the cavity boundary, $(0.2–0.3)c$ in our case. In our $\xi = 0.5$ model the mean wind magnetization is as high as 2.5×10^{-2} (see equation 6); in this case the solution shows signs of oscillatory behaviour, which may be related to the existence of the upper boundary of σ in the Emmering–Chevalier model. This oscillatory behaviour is clearly seen in Fig. 5 in the neighbourhood of the termination shock.

Finally, Fig. 6 shows tongues of the envelope plasma entering the low-density plerionic nebula. Such behaviour is expected as the result of the Rayleigh–Taylor instability at the envelope–nebula interface. The fact that these tongues are most prominent near the equatorial plane and the polar axis seems to indicate that the development of this instability is strongly affected by anisotropy of the global flow in the nebula.

5 SYNCHROTRON EMISSION

The observed synchrotron emission is produced by high-energy non-thermal particles whose evolution, including acceleration, diffusion and energy losses, was not accurately taken into account in our simulations. Instead, we used the following simple model. Let us assume

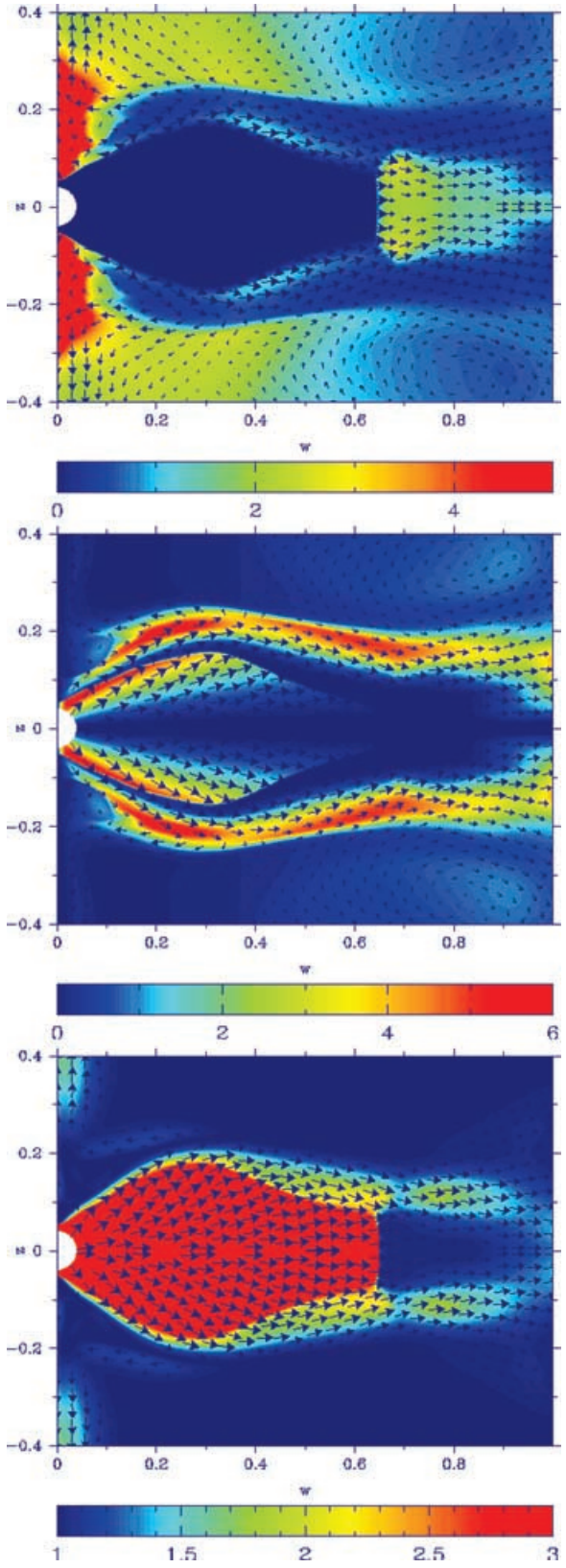

Figure 3. The termination shock complex of the $\xi = 0.5$ model at $t = 170$. Top panel: Gas pressure and velocity vectors. Middle panel: The ratio p_m/p_g and velocity vectors. Bottom panel: Lorentz factor and velocity. In these figures, as well as in other figures throughout this paper, the top and/or bottom values of the colour scale show not the real maximum and minimum values of the parameter shown but the saturation levels of the colour scale.

that the relativistic electrons and positrons have a pure power-law energy distribution, $N(E) = N_0 E^{-p}$, with $p = 2.2$ corresponding to the observed X-ray spectrum of the Crab. In this case, the synchrotron emissivity as measured by an observer at rest relative to the pulsar is

$$\epsilon_\nu \propto N_0 D^{2+\alpha} (B'_\perp)^{\alpha+1}, \tag{7}$$

where $\alpha = (p-1)/2$,

$$D = \frac{\nu}{\nu'} = \frac{1}{\gamma(1 - \boldsymbol{n}\cdot\boldsymbol{\beta})} \tag{8}$$

is the Doppler factor, $\boldsymbol{n}$ is the unit vector pointing towards the observer, $\boldsymbol{\beta} = \boldsymbol{v}/c$ is the fluid velocity as measured in the observer frame, $B'_\perp$ is the component of magnetic field perpendicular to the unit vector $\boldsymbol{n}'$ pointing towards the observer in the fluid frame, and $\boldsymbol{n}'$ and $\boldsymbol{n}$ are related via

$$\boldsymbol{n}' = D\left\{\boldsymbol{n} + \boldsymbol{\beta}\left[\frac{\boldsymbol{\beta}\cdot\boldsymbol{n}}{\beta^2}(\gamma - 1) - \gamma\right]\right\}. \tag{9}$$

To take into account the synchrotron losses we simply introduce an additional factor, $\exp[-(t - t_{\rm inj})/t_c]$, where t_c is the cooling time. Moreover, we assume that N_0 is proportional to the gas pressure. This takes into account, to some extent, the variation of specific volume. Thus, the actual equation for the synchrotron emissivity we used is

$$\epsilon_\nu = \text{constant} \times p_g D^{2+\alpha} (B'_\perp)^{\alpha+1} \exp[-(t - t_{\rm inj})/t_c]. \tag{10}$$

The synchrotron cooling time is given by

$$t_c \approx \frac{6 \times 10^{11}}{\sqrt{B^3 \nu}}.$$

Using the typical magnetic field strength in the central part of the equatorial outflow, $\approx 4B_0 \approx 1.8 \times 10^{-4}$ G (see Fig. 3), we find that in the *Chandra* band $t_c \approx 10 T_0$ (we used $\nu = 7 \times 10^{17}$ Hz, which corresponds to 2.7 keV) and in the optical band $t_c \approx 350 T_0$, which exceeds the computational time. In addition, we forced $\epsilon_\nu = 0$ in the wind zone and, thus, the synchrotron emission originates only from the shocked plasma.

Fig. 7 shows the simulated X-ray maps for the $\xi = 0.5$ model at different epochs for the same angle between the line of sight and the polar axis as derived for the Crab and the Vela nebulae, 60° (Weisskopf et al. 2000; Helfand et al. 2001). Since the flow structure in this model is highly variable (see Section 4), its X-ray appearance varies too. Fig. 8 shows the simulated X-ray maps for the $\xi = 0.2$ model (this solution does not show such a dramatic variability as the $\xi = 0.5$ model) at different viewing angles. Notice that these maps have no component corresponding to the pulsar itself and that the emissivity is set to zero within the termination shock. Thus all features seen in these maps originate downstream of this shock.

In all cases the simulated X-ray images show a system of rings that make an impression of a disc-like or sometimes even a toroidal structure. Its surface brightness rapidly decreases with distance from the centre as a result of a combination of three factors: (1) the synchrotron ageing, (2) the decline of gas pressure, and (3) the decline of magnetic field strength in the equatorial outflow with distance from the pulsar.

The disc surface brightness is lower on the jet side (which is in the lower half of the images) as the result of Doppler beaming, which is the only reason for the breakdown of mirror symmetry with respect to the x-axis.

The most prominent feature of the disc is a very bright arc in its upper half. We will refer to this as the 'main arc'. In the middle

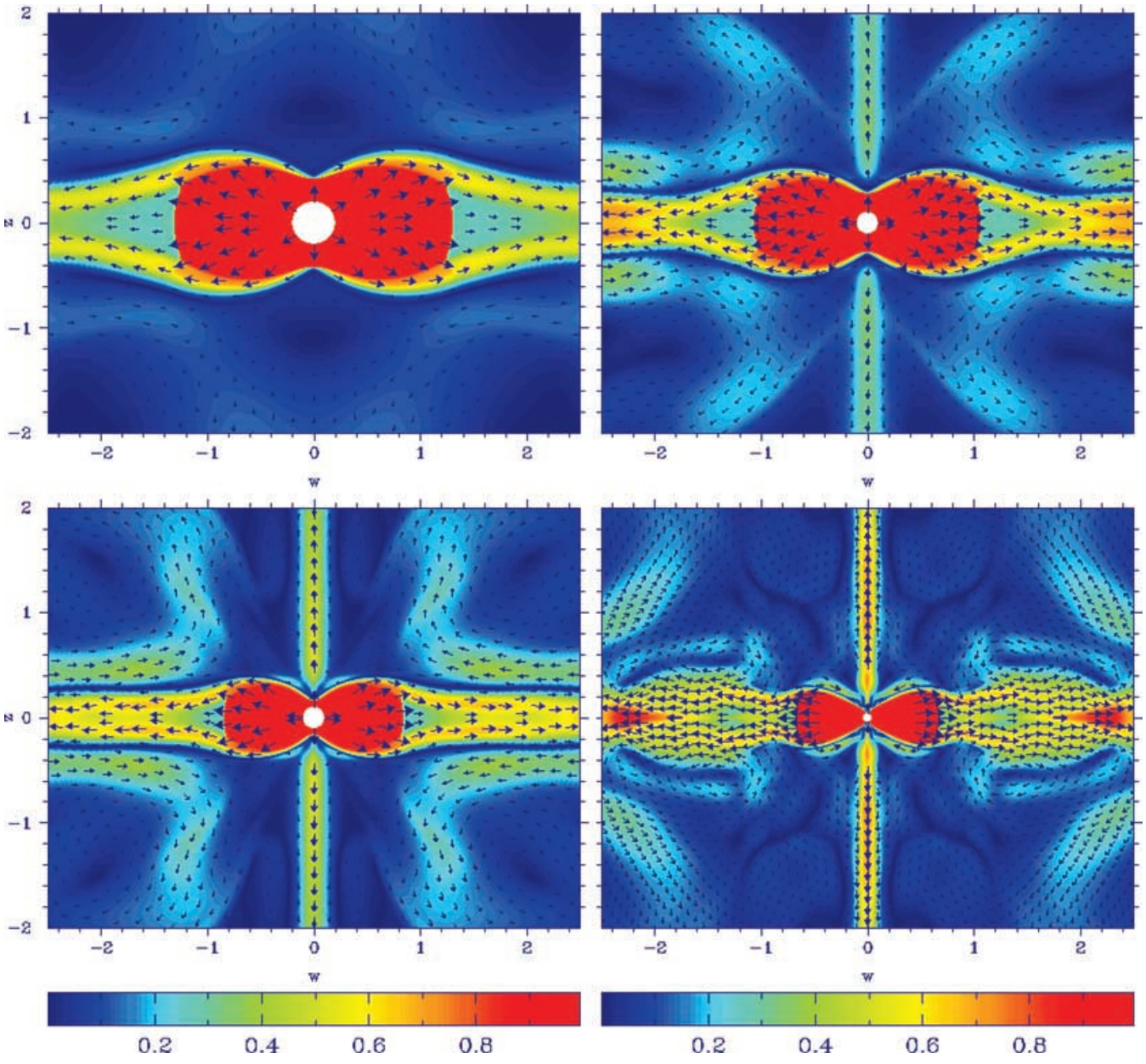

Figure 4. Velocity distribution near the termination shock at $t = 190$ for models with $\xi = 0.1$ (top left), $\xi = 0.2$ (top right), $\xi = 0.3$ (bottom left) and $\xi = 0.5$ (bottom right).

map for the $\xi = 0.2$ model it is located at $y \approx 1.0$ and extends from $x \approx -1$ to $x \approx +1$ (see Fig. 8). Its origin is explained in Fig. 9. As one can see, there are two regions in the Υ stream where the velocity vector points almost directly towards the observer. Since the flow in the Υ stream is still relativistic (see Section 4), the synchrotron emission from these regions is subject to strong Doppler boosting. The main arc is identified with region 2 in this sketch.

In some of the maps, the main arc appears to be attached to one of two almost identical and very thin rings of emission encircling the centre. These 'central rings' originate from the pair of rim shocks discussed in Section 3. In Fig. 9 they are designated by the letter 'R'. Since they indicate the position of the Mach belt, the most distant part of the termination shock complex, they provide a convenient reference for identification of all other features. The Mach belt itself is not a prominent feature because of its relatively low magnetic field and weak Doppler boosting. Other rings of emission seen in Figs 7 and 8 further away from the centre originate in the equatorial outflow.

All simulated maps reveal a bright central source which has nothing to do with the emission from the pulsar itself. Since the emissivity is set to zero within the termination shock, all features seen in these maps originate downstream of this shock. In fact, the central source has two components. The brightest component is produced by the Doppler-boosted emission from the region of the Υ flow shown in Fig. 9 as region 1. In physical space, this region is located much closer to the pulsar than region 2. In the plane of the sky, it is seen even closer than it really is because of the shape of the arch shock (see Fig. 9). Moreover, unless the viewing angle is smaller than the angle between the arch shock and the polar axis in the cusp

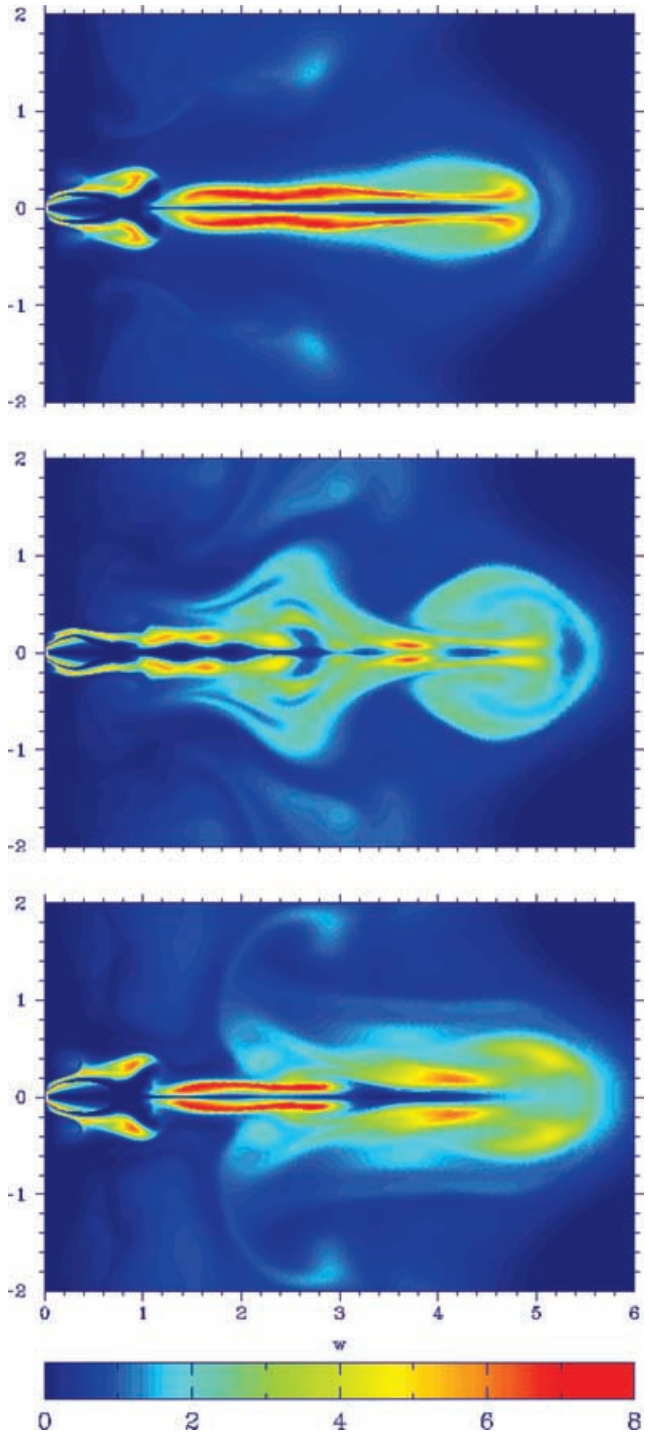

Figure 5. Variability of the disc flow in the $\xi = 0.5$ model. The solution is shown at $t = 150$ (top panel), $t = 170$ (middle panel) and $t = 180$ (bottom panel). The displayed parameter is the ratio of magnetic and gas pressures.

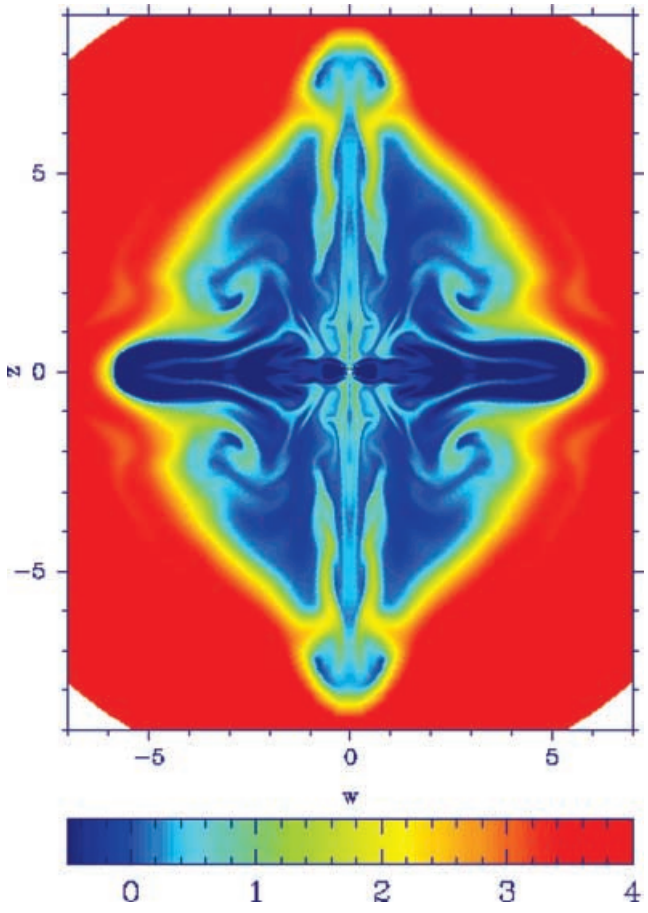

Figure 6. Proper density distribution for the $\xi = 0.5$ model at $t = 190$ (logarithmic scale).

region of the shock, this component appears on the jet side of the polar axis (see Fig. 10).

Another weaker component of the central source is produced by the emission of the high-pressure regions at the base of the polar jets. Since the flow velocity in these regions is rather small, this component is more or less symmetric relative to the x-axis. It becomes relatively more prominent in models with higher wind magnetization. The symmetric central component of the map shown in the upper panel of Fig. 7 seems to have this origin.

Finally, the rather thin and faint jet-like features seen in Figs 7 and 8 correspond to the polar jet approaching the observer. The counter-jets are hardly seen at all in these maps.

The most bizarre map of the $\xi = 0.5$ model, reminiscent of a car wheel (the middle panel of Fig. 7), is shown again in Fig. 11 but now using the linear scale. In this presentation it looks remarkably similar to the *Chandra* map of the Vela nebula (Helfand et al. 2001; Pavlov et al. 2001, 2003).

6 DISCUSSION

The discovery of the 'jet–torus' structures in the pulsar wind nebulae was so unexpected that it prompted calls for the revision of their theory. The most radical of these proposes to abolish the MHD approximation altogether and to develop a purely electromagnetic model (Blandford 2002; Michel 2004). The results of numerical simulations presented in Sections 3 and 4 convincingly demonstrate that the 'jet–torus' structures can be explained, at least in principle, within the framework of the magnetohydrodynamic approach provided one allows for the anisotropy of pulsar winds. Moreover, the apparent likeness between the simulated and the observed X-ray images of pulsar nebulae exceeded our most optimistic expectations.

Indeed, the simulated images show a system of rings, which gives the impression of a disc-like or even a toroidal structure, and jets aligned with the rotational axis of the pulsar. In good agreement

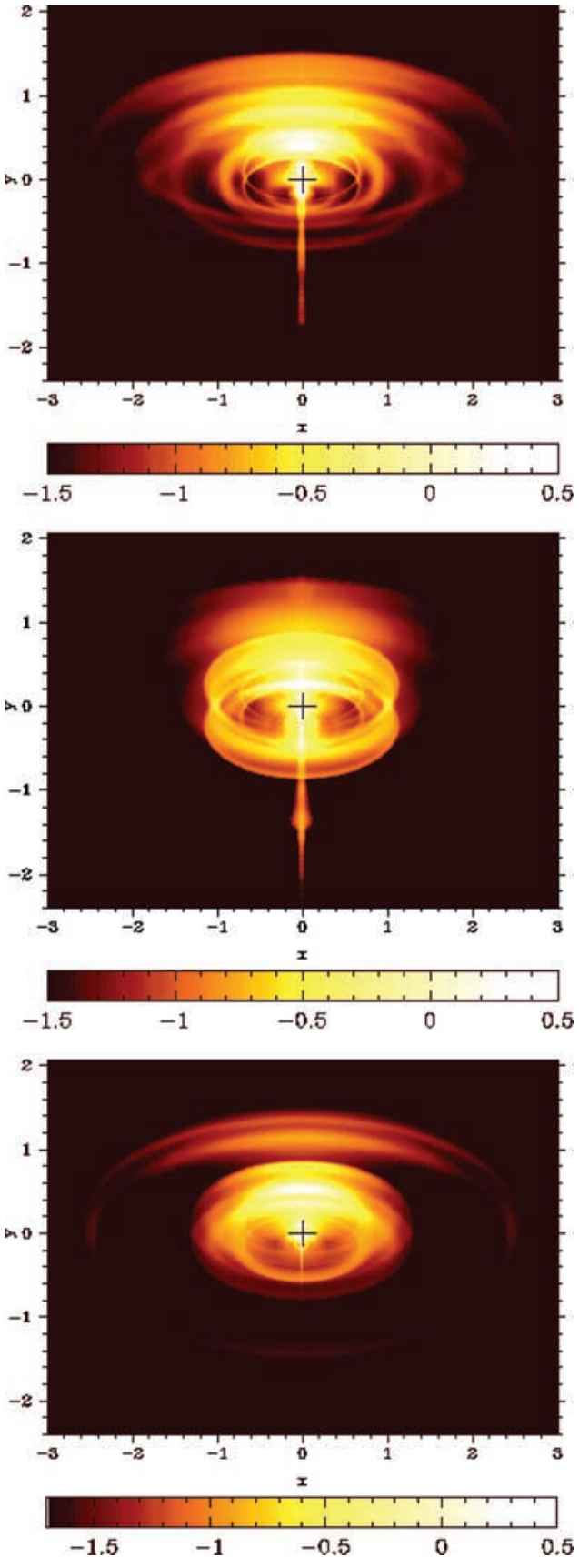

Figure 7. Synchrotron X-ray images for $\xi = 0.5$ model at different epochs: $t = 170$ (top), 180 (middle) and 190 (bottom). The viewing angle is 60°. Note that the X-ray brightness is shown using logarithmic scale.

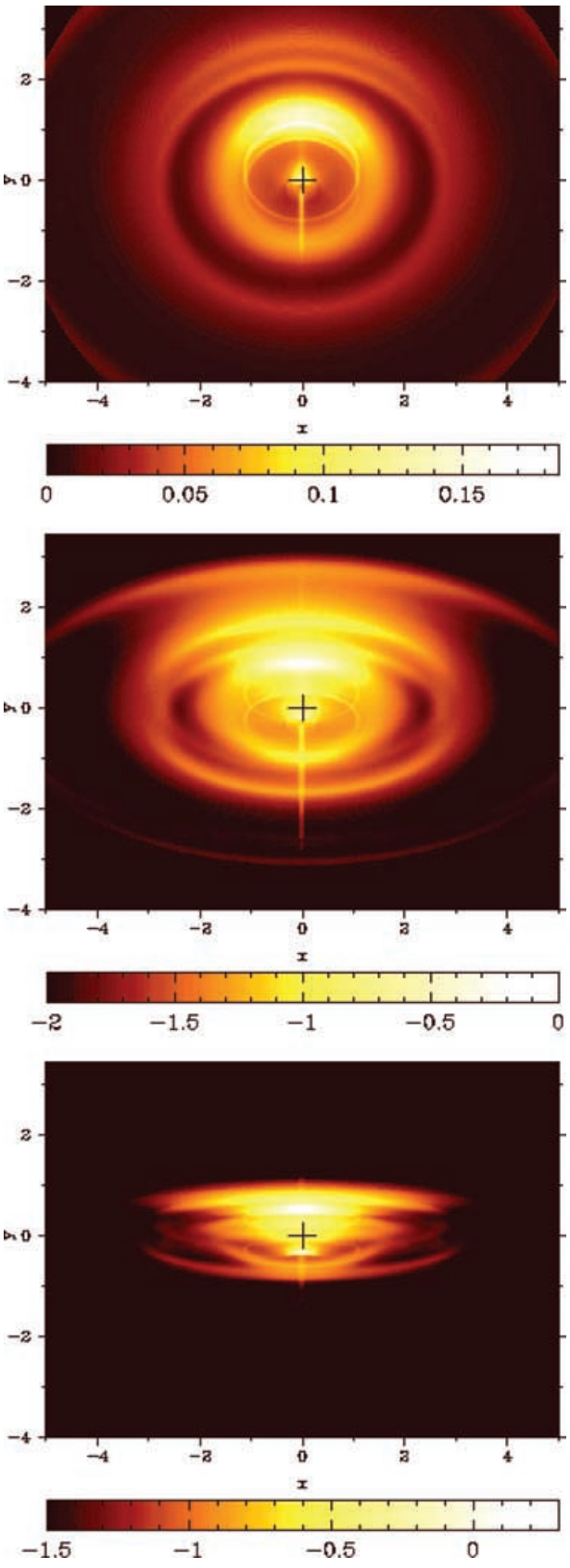

Figure 8. Synchrotron X-ray images for $\xi = 0.2$ model at $t = 190$. The viewing angle is 30° (top), 60° (middle) and 80° (bottom). Note that in the top image the X-ray brightness is shown using a linear scale whereas the other images have a logarithmic scale.

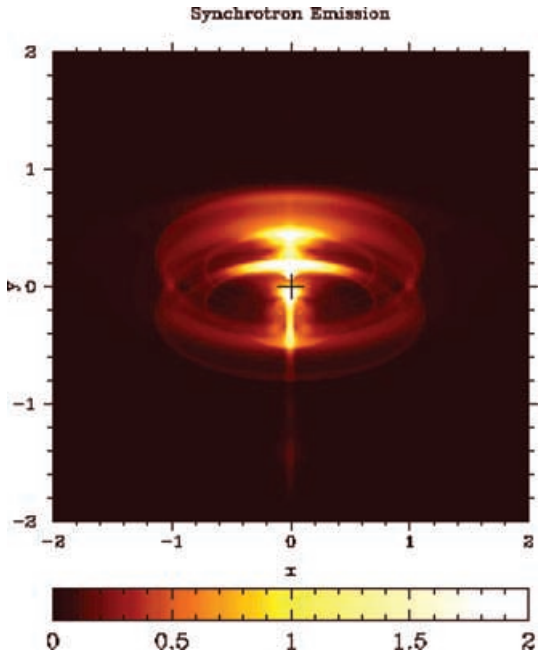

Figure 9. Synchrotron X-ray image for $\xi = 0.5$ model at $t = 180$. The viewing angle is 60°. This image is shown using a linear scale.

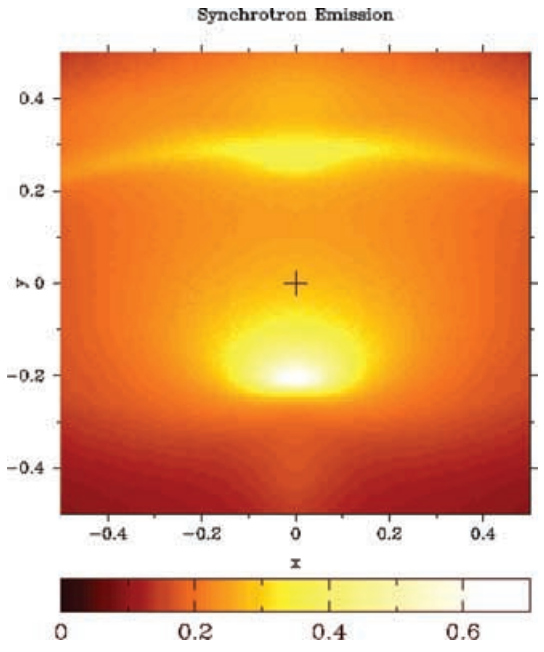

Figure 10. Central part of the optical image for $\xi = 0.2$ model at $t = 190$. The viewing angle is 60°. This image is shown using a linear scale.

with the observations, the rings are brighter on the counter-jet side (Weisskopf et al. 2000; Helfand et al. 2001). In our model, this asymmetry, as well as the brightness contrast between the jet and the counter-jet, is caused by the Doppler beaming effect.

The central source located in the simulated maps close to the position of the pulsar is an invariably bright feature of these maps and must have an observational counterpart if our model is correct. So, we have thoroughly studied the published images of the Crab nebula in the search for such a counterpart and we believe that we have found one. We believe that it is the very bright 'knot' discovered by Hester et al. (1995) 0.65 arcsec to the south-east of

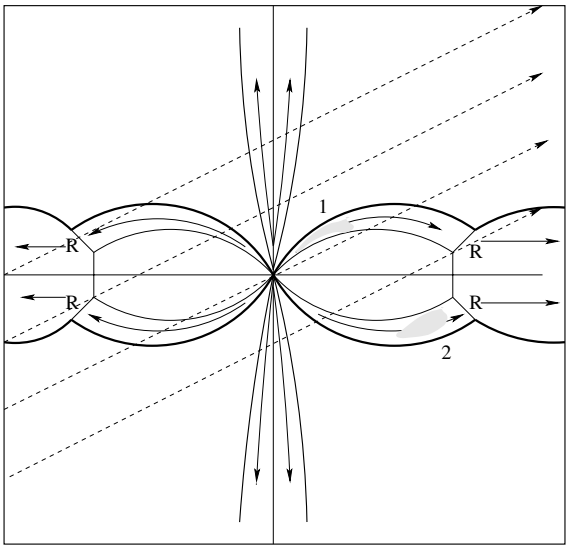

Figure 11. Origin of the brightest features in the simulated X-ray images in Figs 7–9. Here the dashed lines point towards the distant observer. In the shaded regions 1 and 2 the flow velocity is aligned with the line of sight; the synchrotron emission from these regions is strongly Doppler-boosted. These are identified with the 'central source' and the 'main arc' in the simulated X-ray maps. Letter R shows the high-pressure regions just downstream of the 'rim shocks', which give rise to the thin inner rings of the maps.

the Crab pulsar. Fig. 10 shows the central part of the optical image for the $\xi = 0.2$ model at $t = 190$ for the same viewing angle as in the Crab. This image is remarkably similar to the *HST* image shown in fig. 7 in Hester et al. (1995). In both maps the central knot is located along the jet axis. In both maps it is on the same side of the pulsar as the main jet. In both maps it is elongated in the direction perpendicular to the jet axis. In our model, all these properties are determined by the toroidal shape of the arch shock and the Doppler beaming effect (see Section 5). Finally, both images show a thin wisp on the counter-jet side of the pulsar. In our model, this wisp corresponds to the rim shock of the termination shock complex.

Just like in the X-ray maps of the Crab nebula, the simulated jets appear to originate from the pulsar. Their velocity ($\approx 0.5c$, see Section 3) is very similar to that inferred from the observations of proper motion in the jets of both the Crab (Hester et al. 2002) and the Vela (Pavlov et al. 2003) nebulae.

The proper motion of the famous wisps of the Crab nebula indicate an outflow with velocity of $\approx 0.5c$ within the X-ray torus (Hester et al. 2002). This is consistent with the typical value of velocity in the equatorial outflow beyond the Mach belt found in our simulations (see Section 3). The slowing down of these wisps near the outer edge of the X-ray torus reported by Hester et al. (2002) could well be related to the magnetic braking of the surface layers of the equatorial outflow discussed in Section 3. Although in the inner layers of the equatorial disc the magnetic braking is not that effective, these layers are less luminous as a result of their weak magnetic field. Observations indicate that wisps emerge directly from the vicinity of the inner ring of the Crab nebula (Hester et al. 2002), which we tentatively identify with the Mach belt of the termination shock complex. This property also has a natural explanation in our model, as the emission from the Υ flow is largely beamed away from the line of sight.

The nature of moving wisps, however, remains uncertain. They could be easily produced if the pulsar wind was not stationary

(e.g. Lou 1998). Alternatively, they could arise as the result of MHD instability in the flow downstream of the termination shock (Begelman 1999). In fact, the high-pressure cusp region at the base of the polar jet may well be the source of strong perturbations. Indeed, our simulations show that this is not just a stagnation zone but a rather active region exhibiting unsteady vortex motions (see Fig. 3). Notice, however, that numerical viscosity and diffusion efficiently dump short-wavelength perturbations quickly moving relative to the grid. This suggests that proper wisps may be found only in simulations with much higher spatial resolution.

Alternatively, the wisps may originate via physical processes totally ignored in our model. In fact, most of the proposed explanations for the wisps are based on effects, such as finite Larmor radius of ultrarelativistic ions (Gallant & Arons 1994; Spitkovsky & Arons 2000), synchrotron instability (Hester 1998) or drift instability (Chedia et al. 1998), that are not accommodated within the framework of ideal MHD.

One of the important quantitative parameters of the model, which can be tested against observations, is the ratio of the characteristic sizes of the termination shock, l_s, and the nebular cavity, l_c. Assuming that in the Crab nebula l_s is given by the radius of the so-called 'inner ring' and l_c by the equatorial size of the radio image at $\lambda =$ 20 cm (Wilson et al. 1985), this ratio is $l_s/l_c \approx 0.05$. In the $\xi = 0.3$ model we have $l_s/l_c \approx 0.12$, which is significantly higher. However, for numerical reasons, the expansion speed of the simulated nebula is set to be about four times higher than the observed speed, and this prohibits direct comparison. In order to account for this difference in v_c, one has to know how the solution scales with v_c. In the gas dynamic limit, it is found (Rees & Gunn 1974) that

$$l_s/l_c \approx \sqrt{v_c/c}. \tag{11}$$

Assuming that in the case of weakly magnetized winds l_s/l_c still scales as $\sqrt{v_c}$, we find that for the Crab's value of v_c this ratio would be $l_s/l_c \approx 0.06$, which is close to the observed ratio.

Similar scaling can be used to deduce the magnetic field strength we would have if we used the Crab's value of v_c. According to equation (4) one has to multiply our value of B by an additional factor of 2. For the $\xi = 0.3$ model this gives us $B \approx 150$ μG in the main body of the nebula and up to ≈450 μG in the upper layers of the Υ stream. These numbers can be compared with the observational data. The standard equipartition estimate based on radio data (Wilson et al. 1985) yields 330 μG for the mean value of magnetic field in the radio nebulae. The same magnetic field is necessary to explain the synchrotron cooling break in the spectrum at about 10^{13} Hz (Marsden et al. 1984). The analysis of the ultrahigh-energy γ-ray radiation, presumably originating from the inner part of the nebula, delivers 150–200 μG (Hillas et al. 1998; Aharonian & Atoyan 1995).

All these results show that our model captures many properties of the Crab nebula quite well. However, given the high degree of uncertainty in the pulsar wind model, one would still expect to see at least some quantitative differences with the observational data. Indeed, there are such differences.

Some of them are clearly caused by the condition of exact axisymmetry. For example, the optical/radio images of the simulated nebulae produced under the assumption of negligible synchrotron losses are rather different from the observed images. Indeed, they reveal strong elongation along the rotational axis which reflects the global Z-pinch structure of the pulsar nebula. In three-dimensional simulations, the kink instability would destroy this structure, allowing the magnetic loops to come apart and, hence, to reduce the axial compression of the nebula (Begelman 1998). Apparently for the same reason, the Crab's jet is not so straight and well collimated as its numerical counterparts and it does not extend that far away from the pulsar. Instead, it bends, spreads and eventually merges into the surrounding plasma. 3D simulations are needed to study the effect of kink instability of the jet propagation and the mechanism of its production.

The simulated X-ray jets are also rather faint compared to the observations. This may be explained by the fact that the magnetic field in our simulations is purely azimuthal. As a result, it vanishes on the symmetry axis and so does the synchrotron emissivity. In a 3D case, the strong velocity shear would generate the poloidal component of magnetic field in the jet, thus increasing its synchrotron emissivity. In fact, in order to make the jets as prominent as they are in Figs 7 and 8, we artificially introduced the poloidal component of the magnetic field within the jet volume at the level of 30 per cent of the gas pressure. Otherwise, the jets, though still seen in the maps, would be noticeably weaker.

Another important difference is the much higher brightness contrast between the jet and the counter-jet sides of the inner rings in the simulated maps. The observations show that brightness contrast between the opposite north-west and south-east parts of the Crab torus is only about 3 (Greiveldinger & Aschenbach 1999; Weisskopf et al. 2000), whereas in the simulated maps it is as high as 10–15. Since in our model this asymmetry is entirely due to the relativistic beaming, it strongly depends on the velocity field close to the termination shock. In fact, the brightest features of the simulated maps originate in the Υ stream where velocity is as high as (0.8–0.9)c (see Section 3). Such a high velocity is explained by the fact that the arch shock is very oblique as the result of the high asymmetry of the energy flux distribution in the pulsar wind (see equation 1). This allows us to speculate that the Crab's wind is less asymmetric than the wind of the split-monopole model (Michel 1973; Bogovalov 1999). Another possibility is even higher magnetization in the polar region of the pulsar wind leading to even more effective magnetic braking downstream of the arch shock. Indeed, in the $\xi = 0.5$ model the brightness contrast is less than in other models. In any case, the brightness asymmetry of the Crab's 'torus' imposes strong observational constraints on the pulsar wind models.

In the context of our MHD model, the most puzzling feature of the Crab X-ray image is its so-called 'inner ring' (Weisskopf et al. 2000), which is often identified with the wind termination shock (e.g. Hester et al. 2002). This ring is even more symmetric than the torus, implying almost zero flow velocity. This is rather difficult to explain in any ultrarelativistic shock model, as even in the purely gas dynamic limit the post-shock velocity of such a shock cannot be less than $c/3$ (Landau & Lifshitz 1959). Given this velocity and the orientation of the Crab pulsar relative to the line of sight, the brightness contrast would have to be about 2. This problem could be resolved if the wind velocity in the equatorial plane was not ultrarelativistic but subrelativistic, though it is hard to see how this could be arranged. Another remarkable property of the ring is its knotty structure (Weisskopf et al. 2000). If the pulsar wind is axisymmetric, then the only way to explain these knots is via some kind of instability in the post-shock flow. The e-folding time of such an instability must be very short. Moreover, such knots are much fainter in the optical maps and, thus, this instability must somehow affect the spectral properties of the nebular emission at high frequencies, e.g. via changing the position of the cut-off frequency in the synchrotron spectrum.

The observations of the Crab nebula show that its radio image is somewhat larger than its optical image in all directions (e.g. Amato et al. 2000). Given the fact that the traveltime of the equatorial flow from the termination shock to the envelope is much shorter than the

optical cooling time, these observations are hard to explain in our model. It could be that the equatorial flow slows down due to the interaction with the line-emitting filaments, which is not taken into account in our simulations.

Finally, we did not take into account the effect of synchrotron cooling on the overall expansion of the nebula. This effect may be quite significant because the observed gas pressure of the nebula is dominated by the optical/ultraviolet electrons whose synchrotron cooling time is comparable with the lifetime of the nebula. However, this is unlikely to have a strong impact on the structure of the inner part of the nebula, which is the main focus of this paper.

7 CONCLUSIONS

Although the problem of pulsar winds remains largely unsolved, there are a number of basic features of such winds that seem to be generally agreed upon:

(i) The wind is radial and its overall structure in the far zone is axisymmetric with respect to the rotational axis of the pulsar.
(ii) The energy flux is at a maximum in the equatorial plane.
(iii) The mean magnetic field of the wind is azimuthal and vanishes in the equatorial plane.

As a result, the average magnetization of the wind and the local magnetization in the equatorial zone, where most of the energy is transferred, may be rather low, well in line with conventional wisdom. However, in the polar region it may have a magnetization high enough for the collimating magnetic hoop stress to become dynamically important downstream of the termination shock. We have constructed a model of the pulsar wind that has all such properties and studied the interaction of such a wind with a freely expanding supernova ejecta via axisymmetric relativistic MHD simulations.

The main properties of the numerical solutions are as follows:

(i) The termination shock is highly non-spherical. It is significantly closer to the pulsar in the polar zone than in the equatorial plane. In fact, this is not a single shock but a complex of several quasi-steady shocks.
(ii) The post-shock flow is far from being quasi-radial, in contrast to the usual assumption of many analytical models. Most of the shocked plasma is initially confined to the equatorial outflow and only later returns back to the main volume of the nebula.
(iii) If the wind magnetization is not very low, the magnetic hoop stress halts the surface layers of the equatorial outflow already in the inner region of the nebula, then pushes its plasma back towards the axis and finally squeezes it along the axis in the form of magnetically collimated jets, just like was proposed in Lyubarsky (2002). The transition from the 'lonely torus' morphology to the 'jet–torus' morphology occurs at the mean magnetization parameter $\sigma_{\rm m} \approx 4 \times 10^{-3}$, which is only slightly higher than the previously found estimates for the Crab wind, which are based on rather simplistic theoretical models (Kennel & Coroniti 1984; Emmering & Chevalier 1987; Begelman & Li 1992).
(iv) The simulated synchrotron images of plerionic nebulae are strikingly similar to the *Chandra* and *HST* images. The model seems to be able to explain not only the overall structure of the inner Crab nebula but also a number of fine details, such as the typical velocity of its wisps and jets, the fact that wisps seem to emerge from the vicinity of the inner ring and their slowdown within the Crab torus. 'The icing on the cake' is the very confident identification of the 'knot 1' discovered by Hester et al. (1995) with the inner part of the arch shock.

All these results allow us to conclude that the MHD model of pulsar wind nebulae is basically correct. Further studies will clarify the role of the simplifying assumptions made in this work and may even reveal certain deficiencies of the MHD model. However, it seems highly unlikely that the basic elements of the theory will undergo major revision in the future.

When this paper was almost completed we became aware of a similar numerical study being carried out by L. Del Zanna, Amato & Bucciantini (2004), who seemed to use a rather similar setup and have obtained very similar results. This is an important confirmation, which is always welcome in studies involving highly sophisticated computer simulations.

ACKNOWLEDGMENTS

YEL thanks Elena Amato, Jonathan Arons, Ives Gallant, John Kirk, Andrew Melatos, Anatoly Spitkovsky and, especially, David Eichler for valuable discussions and acknowledges support from the Arnow Chair of Physics. SSK acknowledges limited support from PPARC.

REFERENCES

Aharonian F. A., Atoyan A. M., 1995, Astropart. Phys., 3, 275
Amato E., Salvati M., Bandiera R., Pacini F., Woltjer L., 2000, A&A, 359, 1107
Begelman M. C., 1998, ApJ, 493, 291
Begelman M. C., 1999, ApJ, 512, 755
Begelman M. C., Li Z.-Y., 1992, ApJ, 397, 187
Beskin V. S., Kuznetsova I. V., Rafikov R. R., 1998, MNRAS, 299, 341
Blandford R. D., 2002, in Giffanov M., Sunyaev R., Churazov E., eds, Proc. MPA/ESO, Lighthouses of the Universe: The Most Luminous Celestial Objects and Their Use for Cosmology. Springer-Verlag, Berlin, p. 381
Bogovalov S. V., 1999, A&A, 349, 1017
Bogovalov S. V., 2001, A&A, 367, 159
Bogovalov S. V., Aharonian F. A., 2000, MNRAS, 313, 504
Bogovalov S. V., Khangoulyan D. V., 2002a, Astron. Lett., 28, 373
Bogovalov S. V., Khangoulyan D. V., 2002b, MNRAS, 336, L53
Bogovalov S. V., Tsinganos K., 1999, MNRAS, 305, 211
Brinkmann W., Aschenbach B., Langmeier A., 1985, Nat, 313, 662
Bucciantini N., Blondin J. M., Del Zanna L., Amato E., 2003, A&A, 405, 617
Chedia O., Lominadze J., Machabeli G., McHedlishvili G., Shapakidze D., 1997, ApJ, 479, 313
Chiueh T., Li Z.-Y., Begelman M. C., 1998, ApJ, 505, 835
Coroniti F. V., 1990, ApJ, 349, 538
Del Zanna L., Amato E., Bucciantini N., 2004, A&A, submitted
Emmering R. T., Chevalier R. A., 1987, ApJ, 321, 334
Gaensler B. M., Pivovaroff M. J., Garmire G. P., 2001, ApJ, 556, L107
Gaensler B. M., Arons J., Kaspi V. M., Pivovaroff M. J., Kawai N., Tamura K., 2002, ApJ, 569, 878
Gallant Y. A., Arons J., 1994, ApJ, 435, 230
Greiveldinger C., Aschenbach B., 1999, ApJ, 510, 305
Helfand D. J., Gotthelf E. V., Halpern J. P., 2001, ApJ, 556, 380
Hester J. J., 1998, in Shibazaki N., et al., eds, Neutron Stars and Pulsars: Thirty Years After the Discovery. Universal Academy Press, Tokyo, p. 431
Hester J. J. et al., 1995, ApJ, 448, 240
Hester J. J. et al., 2002, ApJ, 577, L49
Hillas et al., 1998, ApJ, 503, 744
Ingraham R. L., 1973, ApJ, 186, 625
Kennel C. F., Coroniti F. V., 1984, ApJ, 283, 694
Kirk J. G., Skjæraasen O., 2003, ApJ, 591, 366
Kirk J. G., Ball L., Skjæraasen O., 1999, Astropart. Phys., 10, 31
Kirk J. G., Skjæraasen O., Gallant Y. A., 2002, A&A, 388, L29
Komissarov S. S., 1999a, MNRAS, 303, 343
Komissarov S. S., 1999b, MNRAS, 308, 1069

Komissarov S. S., Lyubarsky Y. E., 2003, MNRAS, 344, L93
Landau L. D., Lifshitz E. M., 1959, Fluid Mechanics. Pergamon Press, Oxford
Lou Y.-Q., 1998, MNRAS, 294, 443
Lu F. J., Wang Q. D., Aschenbach B., Durouchoux P., Song L. M., 2002, ApJ, 568, L49
Lyubarsky Y. E., 2002, MNRAS, 329, L34
Lyubarsky Y. E., 2003a, MNRAS, 339, 765
Lyubarsky Y. E., 2003b, MNRAS, 345, 153
Lyubarsky Y. E., Eichler D., 2001, ApJ, 562, 494
Lyubarsky Y. E., Kirk J. G., 2001, ApJ, 547, 437
Marsden P. L., Gillett F. C., Jennings R. E., Emerson J. P., de Jong T., Olnon F. M., 1984, ApJ, 278, L29
Marti J. M., Muller E., 1999, Living Rev. Relativ., vol. 2, electronic journal at http://www.livingreviews.org
Michel F. C., 1971, Comments Astrophys. Space Phys., 3, 80
Michel F. C., 1973, ApJ, 180, 133
Michel F. C., 1974, ApJ, 187, 585
Michel F. C., 1982, Rev. Mod. Phys., 54, 1
Michel F. C., 1994, ApJ, 431, 397
Michel F. C., 2004, Adv. Space Res, in press (astro-ph/0308347)
Pavlov G. G., Kargaltsev O. Y., Sanwal D., Garmire G. P., 2001, ApJ, 554, L189
Pavlov G. G., Teter M. A., Kargaltsev O. Y., Sanwal D., 2003, ApJ, 591, 1157
Rees M. J., Gunn J. E., 1974, MNRAS, 167, 1
Sankrit R., Hester J. J., 1996, ApJ, 491, 796
Shibata S., Tomatsuri H., Shimanuki M., K. Saito K., Mori K., 2003, MNRAS, 346, 841
Spitkovsky A., Arons J., 2000, in Kramer M., Wex N., Wielebinski N., eds, Proc. IAU Coll. 177, ASP Conf. Ser. Vol. 202, Pulsar Astronomy – 2000 and Beyond. Astron. Soc. Pac., San Francisco, p. 507
Tomimatsu A., 1994, PASJ, 46, 23
Usov V. V., 1975, Ap&SS, 32, 375
van der Swaluw E., 2003, A&A, 404, 939
Weiler K. W., Panagia N., 1978, A&A, 70, 419
Weisskopf C. et al., 2000, ApJ, 536, L81
Wilson A. S., Samarasinha N. H., Hogg D. E., 1985, in Kafatos M. C., Henry R. B. C., eds, The Crab Nebula and Related Supernova Remnants. Cambridge Univ. Press, Cambridge, p. 133

This paper has been typeset from a TEX/LATEX file prepared by the author.